AIAA JOURNAL
Vol. 59, No. 5, May 2021

Prioritizing Possible Force Models Error in Multiphase Flow Using Global Sensitivity Analysis

Samaun Nili,* Chanyoung Park,† Nam H. Kim,‡ Raphael T. Haftka,§ and S. Balachandar¶
University of Florida, Gainesville, Florida 32611

https://doi.org/10.2514/1.J058657

Modeling gas–particle interaction in an Eulerian–Lagrangian frame involves many approximate models. Hence, understanding the model form error is essential to improve the prediction capability. Often, a model by itself consists of several submodels where each submodel is subject to potential error. The potential errors can superimpose or compensate for each other over time, which makes it difficult to find a possible source of model form error. This study aims to quantify, rank, and isolate the contribution of error in each submodel to the error in the model prediction. The concept of global sensitivity analysis is extended by using it as a tool to isolate the most influential potential error in drag force submodels of a transient multiphase dispersed flow on particle cloud position. The possible errors of the submodels are modeled as uniformly distributed epistemic uncertainty, and their contributions to the quantity of interest are calculated in terms of sensitivity indices. We found that the most influential potential submodel error depends on time and the characteristic of the particle cloud.

Nomenclature

C_M	=	added-mass coefficient
d_i^p	=	particle diameter
E	=	expected value
e_{am}	=	added-mass potential error
e_{ip}	=	interparticle collisional potential error
e_{pg}	=	pressure gradient potential error
e_{qs}	=	quasi-steady potential error
F	=	perturbed force
$f_{\text{am},i}$	=	added-mass force per unit mass
f_{ip}	=	interparticle collisional force model
$f_{\text{pg},i}$	=	pressure gradient force per unit mass
$f_{\text{qs},i}$	=	quasi-steady force per unit mass
f_i^{gp}	=	aerodynamic force from gas to particle per unit mass
f^p	=	total particle force
$\boldsymbol{M}$	=	error sample matrix
M_i	=	particle Mach number
P_1	=	atmospheric pressure
P_2	=	postshock gas pressure
P_{2r}	=	postreflected shock gas pressure
P_{2t}	=	post-transmitted shock gas pressure
Re_i	=	particle Reynolds number
r	=	variable index
S_i	=	first-order effect of X_i
S_{ij}	=	second-order effect index
T_1	=	atmospheric temperature
T_2	=	postshock gas temperature
T_{2r}	=	postreflected shock gas temperature
T_{2t}	=	post-transmitted shock gas temperature
u_1	=	atmospheric gas velocity
u_2	=	postshock gas velocity
u_{2r}	=	postreflected shock gas velocity
u_{2t}	=	post-transmitted shock gas velocity
u_i^g	=	gas velocity at particle location
u_i^p	=	particle velocity
Var	=	variance
V_i	=	first-order partial variance
V_{ij}	=	second-order partial variance
$V_{X_{-i}}(.)$	=	variance due to all input variables except for X_i
V_y	=	model output variance
V_y	=	model output variance
V_i^p	=	particle volume
X_i	=	random variable
x_i^*	=	ith realization of random variable X_i
$x_r^{(N)}$	=	Nth sample of the rth variable
Y	=	model output for a random variable
y	=	realization of model output
$\boldsymbol{y}$	=	realization model output vector
μ_i^g	=	dynamic viscosity at particle location
ρ_i^g	=	gas density at particle location
τ_i^{pp}	=	particle–particle stress
ϕ_i^p	=	particle volume fraction at particle location
ϕ_i^p	=	particle volume fraction at particle location

I. Introduction

PREDICTING the interaction of a shock with a moderately dense distribution of particles is a challenging problem. The shock–particle interaction is essential for understanding the compressible multiphase physics, which applies to many environmental, industrial, and medical applications. To predict the behavior of a system involving shock–particle interaction, numerical simulations are often used. Typical simulations employ point-particle force and heat transfer models to couple the particle momentum and energy with those of the surrounding gas. The models employed in these complex systems often consist of multiple submodels. Hence, the models may be subject to many sources of error from the submodels. It is difficult to identify the dominant source of error since the predicted quantity of interest (QOI) includes the effect of all the submodels errors. For the shock interaction with particle cloud (curtain) problem, the time evolution of a particle curtain (its center of mass and width) depends on the hydrodynamic force exchange between particles and gas and on the interparticle collision force [1,2], and thus serves as a good candidate for evaluating the accuracy of these force models.

Presented as Paper 2017-3800 at the 23rd AIAA Computational Fluid Dynamics Conference, Denver, CO, June 5–9, 2017; received 12 June 2019; revision received 9 March 2020; accepted for publication 26 October 2020; published online 10 March 2021.

*Doctoral Candidate, Department of Mechanical and Aerospace Engineering; samaunnili@ufl.edu. Student Member AIAA.

†Research Scientist, Department of Mechanical and Aerospace Engineering; cy.park@ufl.edu. Member AIAA.

‡Professor, Department of Mechanical and Aerospace Engineering; nkim@ufl.edu. Associate Fellow AIAA.

§Distinguished Professor, Department of Mechanical and Aerospace Engineering; haftka@ufl.edu. Fellow AIAA.

¶Distinguished Professor, Department of Mechanical and Aerospace Engineering; bala1s@ufl.edu.

In this paper, we used global sensitivity analysis (GSA) to identify the potential influential sources of error. GSA has been used to decompose the uncertainty or variance of the model output into the different sources of uncertainty in the model inputs [3,4]. GSA belongs to variance-based sensitivity methods. These methods are formulated based on the conditional variance, and sensitivities can be obtained by Monte Carlo simulation or Latin hypercube sampling (LHS) [5]. The Fourier amplitude sensitivity test indices [6,7] and the Sobol indices [8–10] are commonly used to compute the sensitivity indices, and we chose the latter for this study. We use GSA to identify the possible contribution of the epistemic errors in submodels to the total error in QOI. In this study, we model the possible error of individual submodels as a probability distribution and calculate the contribution of individual errors on the error in QOI. Therefore, this can be considered as an extension of the conventional usage of GSA. There has been much research on the effect of the uncertainty and modeling errors on the model prediction. For instance, Matsumura et al. [11] and Matsumura and Haftka [12] investigated the conservative treatment of model epistemic uncertainty and its reduction using additional knowledge (test data) using the Bayesian framework. They demonstrated that incorporating the effects of future redesign provides significantly better accuracy of the probability of failure estimation. Similarly, Zhang and Mahadevan [13] applied Bayesian failure probability analysis to update the crack growth models with presence of the uncertainty in the model parameters. They illustrated the combination of two competing crack growth models and considered the uncertainty in the statistical distribution parameters for each model.

Another strand of research for error and uncertainty is propagating modeling errors when a system is composed of several models, and each one contributes to the prediction error. In some cases, the interest is also to evaluate the contribution of each propagated error or uncertainty to the final model output variation. The sensitivity analysis is one of the popular methods to quantify the effect of each contribution. Sankararaman et al. [14] investigated the uncertainty quantification and validation of a model for fatigue crack growth. They classified the uncertainties into different types: variability (e.g., material properties), measurement errors, modeling uncertainty and errors, and discretization error. They propagated the uncertainties into the model; then, they quantified the contribution of each source of uncertainty to the overall prediction uncertainty using GSA. They demonstrated that they could use GSA to select the effect of combined uncertainties and errors in the crack growth rate model parameters, the model error by itself, the error in the surrogate model, and the discretization error on the model output variation. Similarly, Burt and Josyula [15] employed GSA for the uncertainty quantification involving mixed aleatory and epistemic uncertainties to compare the impact of multiple input parameters and modeling parameters for a hypersonic shock interaction flow problem. So, they can identify the most responsible parameter for discrepancies between the numerical and experimental data.

Youn et al. [16], Jung et al. [17], and Sankararaman et al. [18] proposed a hierarchical model calibration procedure with a statistical model calibration technique where a system can be decomposed into components. Each component has error or uncertainty. They classified the errors and uncertainties as known and unknown random variables. The known variables can be characterized by observed data or other information such as a product catalog. The unknown variables cannot be directly quantified. Their variability is unknown. However, they can be estimated, i.e., from the expert opinion. This process can be followed by sensitivity analysis and calibration that can reveal the unmodeled phenomena or unknown unknowns.

Three possible methods of quantifying the model error in the literature can be summarized as 1) propagating the error and using the information to redesign the future tests; 2) propagating the model error when the system is composed of different models and observing the output variability, which is often followed by sensitivity analysis to quantify the contribution of an individual component to the output variation; and 3) treating the error as known and unknown variables, propagating it into the model, and observing the response variability, followed by sensitivity analysis and calibration. The method of GSA was previously applied for prioritizing the effect of varying inputs on model output. Sankararaman et al. [14] extended the method and applied it to investigate the effect of data uncertainty, model parameter error, and surrogate error all together on the model output. In this paper, GSA is applied to a problem where the overall model consists of several submodels. Each submodel is subject to a potential error where the model prediction error comes from the combined effect of the potential error in each submodel.

A complex physical model may include several submodels, each of which has its own potential model error. In dynamic systems, the interaction between these submodel errors can evolve over time and make it more difficult to quantify the effect of individual errors on the prediction of QOI. That is, the errors can superimpose or compensate one another over time. The aim of this paper is to isolate the dynamic effect of each potential submodel error on the prediction of QOI and rank them using GSA. The errors on each submodel are propagated simultaneously with the assumption that there is a known error bound for each submodel.

The rest of the paper is organized as follows: Sec. II introduces the background information about the problem of shock–particle interaction, followed by the multiphase shock tube experiment and the numerical simulation. Section III discusses the potential error in the submodels and the need to perform a GSA study on the submodels; followed by Sec. IV, where we discuss the mathematical expression of the submodels. In Sec. V, the ranking of the potential force submodels error using GSA will be discussed, followed by details about applying GSA in the shock–particle interaction problem and the method used to perform GSA. Section VI presents the results, followed by the conclusions in Sec. VII.

II. Physics of Shock–Particle Interaction

This paper deals with the physics of shock interaction with a moderately dense curtain of particles. This problem involves a wide range of length and time scales. For example, the thickness of a shock in the air is of the order of 100 nanometers, whereas particle diameter can be micrometers to millimeters, and the size of the particulate curtain can range from centimeters to meters. Correspondingly, the time scale of shock passage over a particle can be less than 1 μs, whereas the motion of the particulate curtain itself may occur over milliseconds. Given this wide range of length and time scales, with the current computational capability, it is impossible to simulate a fully resolved shock interaction with more than $\mathcal{O}(10^3)$ particles [19–21]. Simulations involving a much larger number of particles must resort to Euler–Euler or Euler–Lagrange techniques, where the details of the flow around each particle will not be fully resolved, and must therefore be modeled appropriately.

Typical simulations thus employ point-particle force and heat transfer models to couple the particle momentum and energy with those of the surrounding gas. To validate the applicability of these models for the problem of shock–particle interaction, the results from a multiphase shock tube (MST) experiment have been used, where a normal planar shock wave passes through a planar curtain of a moderately dense mixture of gas and particles. The time evolution of the curtain (the center of mass and width) depends on the hydrodynamic force exchange between the particles, the gas, and the interparticle collision forces [1,2], and thus serves as a good candidate for evaluating the accuracy of these force models. Therefore, the simulation calculates the time evolution of the particle curtain and compares it against the experiment to evaluate the accuracy of the numerical models. The discrepancy between the experimental measurements and simulation predictions can be translated into the model form error. The length and time scales of our interest in this study are limited to the order of millimeters and microseconds, which is within the limit of MST capability. In the problem of shock–particle interaction, the drag force model is decomposed into several submodels where each submodel is subject to a potential error. The effective error is the combined effect of the possible error on each submodel.

Figure 1 shows the schematic of the MST experiment conducted by Wagner et al. [2,22] at Sandia National Laboratories. The shock tube consists of a driver section, where the high-pressure gas is kept; and the driven section, which is kept under atmospheric conditions. The driven section is separated from the driver section via a diaphragm. When the diaphragm is burst, a planar shock wave is created and

propagates toward the test section due to the pressure difference between the driver and driven sections. The test section is located at the end of the driven section, where the particle curtain can be observed through the glass window. The particle curtain is formed by dropping particles from a reservoir through a slit. Figure 1b shows the schematic zoomed-in view of the particle curtain. Upon the diaphragm burst, the shock wave propagates toward the test section, hits the particle curtain, and passes over them. The particle curtain starts moving and expanding due to the hydrodynamic and interparticle collisional forces. Figure 2 shows the computational schematic of the MST [2]. Figures 2a and 2b show the schematic of the particle curtain before and after the shock impact. P, T, and u indicate the gas the pressure, temperature, and velocity, respectively. The preshock (atmospheric), postshock, postreflected shock, and post-transmitted shock conditions in Figs. 2a and 2b are defined by subscripts 1, 2, 2r, and 2t, respectively. The contact surfaces are not presented in Fig. 2. A detailed figure including the contact surfaces is provided in Ref. [23]. The upstream particle front position (UFP) and downstream particle front position (DFP) are being used to validate the numerical force models in the simulation. Figure 2c shows the time evolution of the UFP and DFP for the particle curtain with the initial thickness of 2 mm, where the particle curtain expanded after being hit by the shock wave.

A one-dimensional (1-D) numerical simulation is used to predict the motion of particles and the evolution of the curtain. The code is a simplified version of a computational fluid dynamics simulation program Rocflu, developed at the Center for Simulation of Advanced Rockets [24]. The Eulerian–Lagrangian approach is used where the underlying flowfield is treated as a continuum and solved on an Eulerian framework, whereas particles are considered as discrete points that move due to interactions with the flowfield and with each other. The simulation is four-way coupled since it includes the effect of particles on the gas as well as the effect of particle–particle interaction. Since the mass or volume loading of particles is significant, the effect of particles on the carrier fluid flow cannot be ignored. In addition, since the particle volume fraction is considerable in our study, the interparticle collision between particles becomes significant. In this study, the particle volume fraction is 21%, and 5000 computational point particles are used where each particle is a sphere with a 115 μm diameter. More details about the particle volume fraction are provided in the Appendix. The locations of averaged leftmost 0.5% and rightmost 0.5% particles are defined as the UFP and DFP, respectively. The details of the numerical method are outlined in Ref. [25].

In evaluating the accuracy of the force models by comparing the simulation results against corresponding experiments, it must be noted that the shock tube experimental results involve unavoidable uncertainties in measurement, such as quantification of experimental conditions, shock Mach number, time of shock arrival, particle size distribution, curtain thickness, particle volume fraction variation within the particle curtain, and measurement of particle front

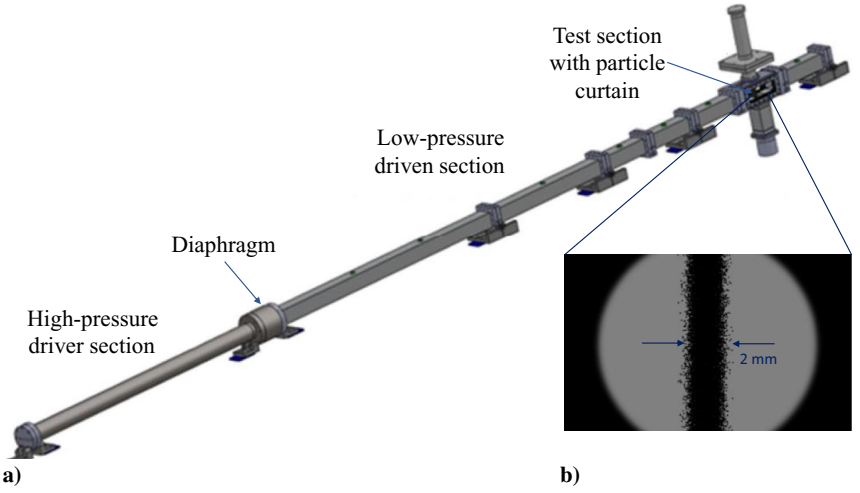

Fig. 1 Schematic of the multiphase shock tube: a) Sandia multiphase shock tube, and b) particle curtain before impact.

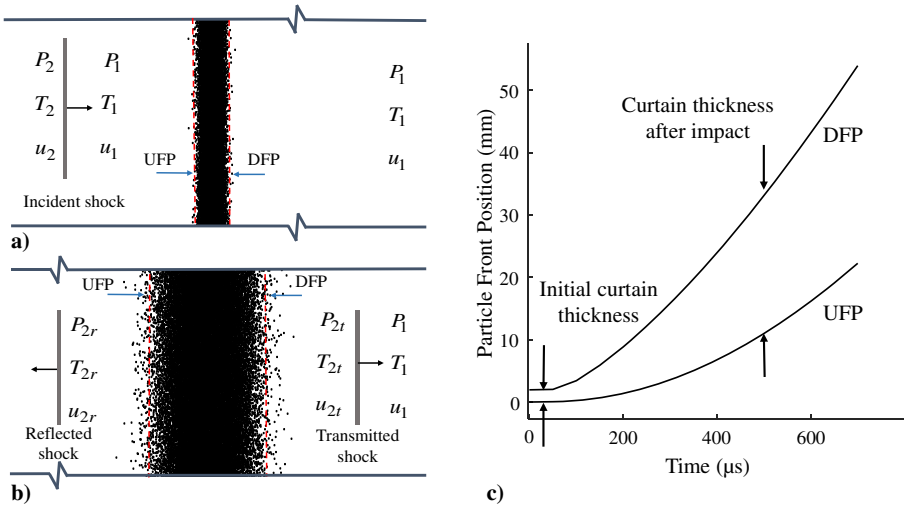

Fig. 2 Schematic of particle curtain a) before impact, and b) after impact. Note the particle curtain moves toward the shock tube downstream after the impact. Figure 2c shows the time evolution of the particle curtain.

positions. Similarly, numerical simulations suffer from errors such as discretization errors in addition to errors in the point-particle force model used to couple the particles and the surrounding gas. If experimental and numerical uncertainties are large, then any attempt to evaluate the performance of the force model will be meaningless. Hence, to enhance the reliability of experimental results and predictive capability of numerical simulations, an elaborate effort of uncertainty reduction is essential.

Park et al. [26,27] performed a rigorous effort of uncertainty reduction of the problem of shock–particle interaction to reveal the model error of the simulation by comparing it to the experimental measurement. Figure 3 shows the time evolution of the numerical simulation of the UFP and DFP after the shock passed over the particles, compared against the experimental measurement. The thickness of the simulation curves shows the effect of the propagated uncertainties within a 95% confidence interval (CI) on the UFP and DFP via 10 simulations. The thickness of the experiment curves in Fig. 3 represents a 95% CI of sampling uncertainty out of four repetitions.

After uncertainty quantification, the remaining discrepancy between the simulation and experiment needs to be explained in terms of errors in force models. To understand the possible sources of error, the effect of these potential errors on the QOI needs to be investigated. Here again, attention will be focused on the force model since heat transfer does not play an important role in this problem. Since important contributors to particle motions and, hence, to the particle curtain motion are quasi-steady, unsteady aerodynamic forces and interparticle collisional forces, quantifying and ranking the influence of the errors in these models on the uncertainty in the UFP and DFP calculations is essential toward improving prediction capability. Nili et al. [28] performed a preliminary version of this study for a different configuration of the problem of interaction of the shock with the particle curtain.

III. Potential Error in the Force Models and Global Sensitivity Analysis

The sensitivity of the particle front motion to the potential force model error is investigated for the problem of interaction of a planar shock wave with a moderately dense particle curtain. The sensitivity analysis is performed in the Euler–Lagrange point-particle approach, where the motion of individual computational particles is traced in a Lagrangian framework, and the particle force models that depend on the volume fraction are used to model the shock–particle interaction. The force model consists of several contributions: quasi-steady, pressure gradient, added-mass, and interparticle collisional force contributions. The expressions of these force models (called submodels here) are well established in the limit of a zero Reynolds number, a zero Mach number, and for an isolated particle: both in the incompressible flow [29] and, more recently, for a compressible flow [30–32].

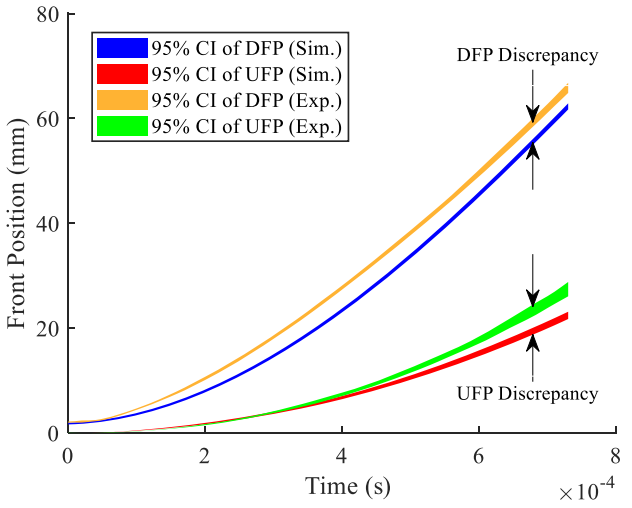

Fig. 3 The effects of input uncertainties and experimental variability on the UFP and DFP. (Sim. denotes simulation, and Exp. denotes experiment.)

However, for the present application of compressible flow (at finite Reynolds and Mach numbers) over a distribution of particles at a moderate volume fraction, the force models are subject to substantial epistemic uncertainty. This is because neither the model form nor the values of any associated coefficients of the quasi-steady, added-mass, and collisional force models are fully understood or settled for this flow regime. The range of uncertainty of the submodels must be estimated. A variance-based global sensitivity analysis allows us not only to rank the effect of potential error in each submodel on the variation of predicted QOI (chosen to be UFP and DFP) but also provides us with valuable information toward reducing these model uncertainties. GSA allows us an efficient uncertainty quantification for errors in the force submodels. GSA quantifies the importance of error in each force submodel on the variation of the front particle movement as a function of time.

IV. Point-Particle Force Models

As discussed earlier, there have been different modeling options that have been pursued in the simulation of shock–particle interaction with a curtain of particles [25,33,34]. In the work, the force coupling formulation outlined by Ling et al. [35,36] is employed. The aerodynamic force per unit mass on the ith particle, which is denoted by f_i^{gp}, can be decomposed into the contribution of individual force models as

$$f_i^{\mathrm{gp}} = f_{\mathrm{qs},i} + f_{\mathrm{pg},i} + f_{\mathrm{am},i} \tag{1}$$

where $f_{\mathrm{qs},i}$, $f_{\mathrm{pg},i}$, and $f_{\mathrm{am},i}$ denote, respectively, the quasi-steady, pressure gradient, and added-mass forces. This method of force decomposition is accurate for an isolated particle in the limit of zero Reynolds and Mach numbers, where the explicit derivation of each term is available in Refs. [30,31]. Parmar et al. [37] and Ling et al. [35] introduced the importance of the unsteady forces of a planar shock tube by extending these models to a finite Reynolds and Mach numbers. These models were extended to a shock–curtain interaction by Ling et al. [25]. The following three equations represent the expression for quasi-steady, pressure gradient, and added-mass force models, respectively [38,39]:

$$f_{\mathrm{qs},i} = 3\pi\mu_i^g d_i^p \left(u_i^g - u_i^p\right)\Phi\left(Re_i, M_i, \phi_i^p\right) \tag{2}$$

$$f_{\mathrm{pg},i} = -V_i^p \left(\frac{\partial p^g}{\partial x}\right)_i \tag{3}$$

$$f_{\mathrm{am},i} = V_i^p C_M\left(M_i^p, \phi_i^p\right)\left[\left(\rho^g \frac{Du^g}{Dt}\right)_i - \frac{d}{dt}\left(\rho_i^g u_i^p\right)\right] \tag{4}$$

In the point-particle model, all the fluid properties are to be interpreted as the undisturbed flow quantities evaluated at the particle center. Gas properties with subscript i, such as u_i^g, ρ_i^g, and μ_i^g, denote the gas velocity, density, and dynamic viscosity interpolated to the particle center location. Quantities such as $(\partial p^g/\partial x)_i$ and $(\rho^g(Dp^g/Dt))_i$ with subscript i indicate that these gas-related quantities have been evaluated and then interpolated to the particle center. In addition, d_i^p is the diameter and V_i^p is the volume of the ith particle. Here, Φ is the empirical quasi-steady drag correction that is a function of particle Reynolds Re_i and Mach numbers M_i. C_M is the added-mass coefficient that is a function of Mach number. In addition, both Φ and C_M are functions of the particle volume fraction, whose dependencies can be found in the work of Ling et al. [25]. The particle–particle collisional force is modeled in terms of an interparticle collisional force model. The model proposed by Harris and Crighton [40] is used for the interparticle interaction as

$$F_i^{\mathrm{pp}} = -\frac{V_i^p}{\phi_i^p}\nabla\tau_i^{\mathrm{pp}} \tag{5}$$

where τ_i^{pp} represents the interparticle stress, which can be found in the work of Enwald et al. [41].

V. Prioritization of the Potential Force Submodel Errors

As discussed in Sec. III, the remaining discrepancy between experiment and simulation results shown in Fig. 3 needs to be explained in terms of errors in the force models. Hence, the effect of these potential errors on the QOI needs to be investigated. The force model calculates the applied force per unit mass of a particle as the sum of all submodel forces as

$$f^p = f_{\text{qs}} + f_{\text{pg}} + f_{\text{am}} + f_{\text{ip}} \tag{6}$$

Note that the interparticle force is also included along with the aerodynamic forces due to the finite particle volume fraction. The force model consists of several submodels where there is a model error associated with each submodel. The pressure gradient and the added-mass forces are dominant when the particles are subjected to a strong pressure gradient, which in turn induces a strong relative acceleration between the particle and the surrounding fluid. The net of the interparticle collisional forces is expected to be dominant in regions where the particle volume fraction is large and shows large variations (i.e., at sharp particle fronts). These submodels have been developed under dilute conditions of low volume fraction, and therefore their errors increase at a higher volume fraction. Furthermore, both the quasi-steady and added-mass forces depend on the Mach number, which has been calibrated for postshock flow Mach numbers less than the critical value (i.e., less than 0.6). Thus, at higher postshock flow Mach numbers, there is increased error, especially at the higher volume fraction. Since these force submodels do not have a linear relationship with the particle motion, the combined errors on individual submodel over time affect the time evolution of the UFP and DFP. The errors can add up or compensate for one another over time. The goal is to isolate the dynamic effect of each submodel error on the prediction of the particle front position.

A. Global Sensitivity Analysis and its Applications

Sensitivity analysis is often named as one of the essential tools for uncertainty quantification. Sensitivity analysis is used to relate the uncertainty in the input variables to the prediction uncertainty. In many cases, researchers are interested in the assessment of the variation in the model output with respect to an input variable, whereas all other input variables are fixed. This method of evaluating the output derivative at the vicinity of an input value is called local sensitivity analysis, where the sensitivity information is only available at a fixed point [42–44]. When the input variables are defined over a wide range, the local derivative at a fixed point may not be accurate and the evaluation of the local derivative over the entire range for all variables may not be practical. Global sensitivity analysis is capable of decomposing the variation of model output in terms of variation or uncertainty of the input variables defined over a range. GSA has a wide range of applications in uncertainty analysis in the field of combustion, reliability analysis, fluid mechanics, and error analysis. Ganguly et al. [45] used GSA to obtain the sensitivity of the periodic input errors for the heterodyne interferometry model. Hosder and Bettis [46] ranked the effect of the uncertainty in the boundary condition on the heat-flux prediction using GSA for a reentry flow model. Pei et al. [47] performed GSA on a spray of engine combustion networks to understand the influence of differences in boundary conditions on specific targets of interest. Liang and Mahadevan [48] used both local and global sensitivity analyses to rank the effect of uncertainties and error from multiple sources, including the model parameters on the final results. Higdon et al. [49] used GSA to identify the important reaction rate on the simulation of high-temperature hypersonic flow. Jiang et al. [50] used both global and local sensitivity analyses for a multidisciplinary aircraft design problem. They identified the important design variables and disciplinary models that need epistemic uncertainty reduction to achieve a better design solution. Huan et al. [51] conducted GSA on a nonreactive jet in crossflow to identify the influential uncertain input parameters to reduce the system stochastics dimension as well as identified the influential model parameters for the calibration. In this study, GSA is used for a model that consists of several submodels with error associated for each submodel. It is of interest to rank and isolate the effect of potential error of each submodel on the overall behavior of the model output over time. Each error varies within a bound estimated by expert opinion.

For this study, it is assumed that each force submodel is subject to a potential epistemic error within a constant range of $\pm 10\%$. Note that the actual error range of each submodel is unknown, and the goal is to understand how the 10% epistemic error on each force submodel affects the motion of the front particle position for a problem of shock–particle interaction. There are various methods to perform GSA. In this study, the variance-based sensitivity analysis is used where the Sobol indices [8] are used for estimating the influence of individual variables or groups of variables on the model output. Figure 4 shows the schematic time evolution of particle front position due to the propagation of the potential force submodels errors. In this figure, each curve (dashed, solid, and dotted) represents three random realizations of particle front position due to the randomly chosen errors within the error ranges of the force submodels. The shadow band represents the particle front position for a very large number of realizations that represent possible front positions concerning the force submodels errors.

B. Global Sensitivity Indices

According to Sobol [10], the variance of model y can be decomposed as

$$V_y = \sum_i V_i + \sum_i \sum_{j>i} V_{ij} + \ldots + V_{12\ldots n} \tag{7}$$

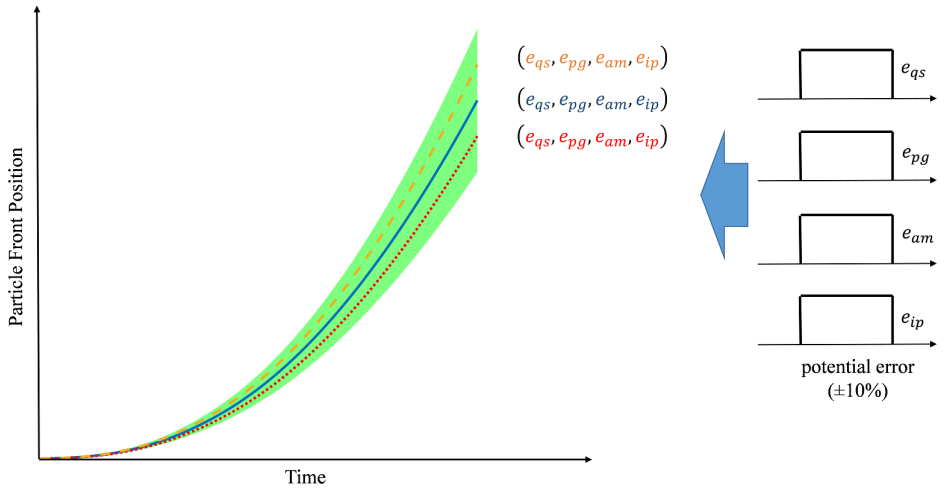

Fig. 4 Schematic of variation in front particle position due to error potential in force submodels.

where V_i and V_{ij} are expressed as

$$V_i = \mathrm{Var}[E(y|x_i)] \quad \text{and } V_{ij} = \mathrm{Var}[E(y|x_i, x_j)] - V_i - V_j \tag{8}$$

V_i is the first-order partial variance that quantifies the effect of variable x_i on the model output variance V_y, whereas the contribution of the second-order interaction between x_i and x_j to V_y is characterized by the second-order partial variance V_{ij}. Similarly, the higher-order interaction effect is measured by higher-order partial variances. In this study, the variable x_i denotes the potential error on the drag force submodels and y represents the QOI, which is the model output, i.e., UFP or DFP. By dividing both sides of Eq. (7) by V_y,

$$1 = \sum_i S_i + \sum_i \sum_{j>i} S_{ij} + \ \ldots \ + S_{12\ldots n} \tag{9}$$

where $S_i = V_i/V_y$ is called the first-order effect of x_i, and $S_{ij} = V_{ij}/V_y$ is called the second-order effect index between x_i and x_j. Saltelli et al. [3] demonstrated a simple and yet practical approach to compute the sensitivity indices for a nonlinear system by taking advantage of statistical sampling.

There are a variety of methods to sample the individual errors on each submodel, including random sampling and the Latin hypercube sampling. For this study, we employ the LHS method. The main advantage of LHS over random sampling is its space-filling characteristics. To perform GSA on the force submodel, the following perturbation is introduced in Eq. (6):

$$F = (1 - e_{\mathrm{qs}})f_{\mathrm{qs}} + (1 - e_{\mathrm{pg}})f_{\mathrm{pg}} + (1 - e_{\mathrm{am}})f_{\mathrm{am}} + (1 - e_{\mathrm{ip}})f_{\mathrm{ip}} \tag{10}$$

where e_{qs}, e_{pg}, e_{am}, and e_{ip} are potential errors related to the corresponding force submodel. Since the errors are unknown, they are modeled as epistemic uncertainty, which represents the lack of knowledge about the force submodels. The uncertain errors are propagated through the numerical simulation to the uncertainty in the particle front positions; that is, potential contributions of the errors in the submodels to the errors in the particle front positions. The potential contributions are measured by their variances. The step-by-step procedure adopted to calculate the sensitivity indices follows the method of Saltelli et al. [3].

First, samples are generated for the potential drag force submodel errors. The variable $x_r^{(N)}$ denotes the Nth error sample of the rth submodel. The following matrix of samples defined

$$\boldsymbol{M} = \begin{bmatrix} x_1^{(1)} & x_2^{(1)} & \cdots & x_r^{(1)} \\ x_1^{(2)} & x_2^{(2)} & \cdots & x_r^{(2)} \\ \cdots & \cdots & \ddots & \cdots \\ x_1^{(N)} & x_2^{(N)} & \cdots & x_r^{(N)} \end{bmatrix} \tag{11}$$

Each row of the matrix $\boldsymbol{M}$ represents an error sample. By using each error sample, the particle front position (i.e., the model output) can be obtained by running the corresponding model. Since there are N samples, the same number of model outputs are obtained as

$$\boldsymbol{y} = \begin{bmatrix} y^{(1)} \\ y^{(2)} \\ \vdots \\ y^{(N)} \end{bmatrix} \tag{12}$$

The variance of the model output is going to be decomposed according to the variance of all input variables and independently from their degree of linearity or monotonicity. According to Saltelli et al. [3], this approach is model free. First, a reduced conditional variance must be obtained, which is the output variance when one of the variables is fixed; that is, the uncertain input is fixed at $X_i = x_i^*$ as

$$V(Y|X_i = x_i^*) \tag{13}$$

In the equation, $V(Y|x)$ represents the conditional variance of Y for a given value of x. The uppercase letters (e.g., X and Y) represent the random variables, and their corresponding realizations are indicated by the lowercase letters (e.g., x and y). Since x_i^* can take any value within the range of X_i, it is possible that $V(Y|X_i = x_i^*) \geq V(Y)$ for a nonlinear model. Therefore, the conditional variance in Eq. (13) is averaged over the distribution of the uncertain variable X_i. The averaged conditional variation is denoted as

$$E[V(Y|X_i)] \quad \text{or} \quad E_{X_i}[V_{X_{-i}}(Y|X_i)] \tag{14}$$

In the equation, $V_{X_{-i}}(.)$ means the variance due to all input variables, except for X_i. Equation (14) has the property that $E[V(Y|X_i)] \leq V(Y)$ and, in particular,

$$\sum_{i=1}^{r} \{E[V(Y|X_i)] + V(E[Y|X_i])\} = V(Y) \tag{15}$$

where $E[V(Y|X_i)]$ is called a residual, and $V(E[Y|X_i])$ is denoted as the first-order effect of X_i on Y. The first-order sensitivity index can be defined as

$$S_{X_i} = \frac{V(E[Y|X_i])}{V(Y)} \tag{16}$$

The first-order effect is large when a variable is influential. The first-order sensitivity indices satisfy the condition of $\sum S_{X_i} \leq 1$, and it is valid for both the linear and nonlinear systems. When the sum of the first-order sensitivity indices is less than one, it means that the remaining variance is due to the interaction between input variables. The contribution due to the interaction between input variables is identified as higher-order indices:

$$S_{X_{i,j,\ldots,n}} = \frac{V(E[Y|X_i, X_j, \ \ldots, X_n])}{V(Y)} \tag{17}$$

Global sensitivity analysis requires many simulations. For this study, there are four potential errors or variables for submodels, where each possesses an error bound. The number of simulations to evaluate the sensitivity index is proportional to its sample population. Each error bound is assumed uniformly distributed with $\pm 10\%$ range, from which 1000 samples are generated. The computer wall time required for a single simulation, on a single core of a standard Intel E5-2698v3 processor with 2.5 GHz clock speed, is about several hours. Therefore, it is necessary to construct a surrogate model to approximate the front particle positions as a function of possible errors in the submodels. A kriging surrogate model [52,53] of front particle position was built based on 42 samples generated using LHS within $\pm 10\%$ error bounds. The number of samples was found to be enough to cover the entire error space. The constructed surrogate model predicts the particle front position for an equal number of time steps in a fraction of a minute.

We examine the accuracy of the surrogate using a cross-validation technique. We performed the cross validation by leaving one point (sample) out at a time and fit the surrogate to the remaining points (e.g., 41 points); then, we checked the error at the left-out points. We repeated the process for all the points (e.g., 42 points), and so we ended up with a cross-validation error at each data point. Table 1 shows the surrogate accuracy of the particle front for a few selected

Table 1 Surrogate accuracy

	Time, μs				
	10	50	100	300	600
UFP PRESS error, mm	1.8e − 5	8.2e − 5	6.1e − 4	2.2e − 3	8.4e − 3
DFP PRESS error, mm	2.4e − 5	3.7e − 4	1.2e − 3	4.0e − 3	2.1e − 2

times. The numbers in Table 1 are expressed as the root mean squares (RMSs) of the cross validation. The term PRESS stands for prediction error sum of squares.

Comparing the PRESS error to the particle front position in Fig. 3 shows that the relative PRESS of the surrogate prediction does not exceed the order of 0.05%.

VI. Results and Discussion

The global sensitivity indices are calculated for both the UFP and DFP at early times and later times. Considering that the shock speed is about 580 m/s, traveling over the entire particle curtain takes less than 4 μs. Therefore, early times are defined as those take up to 10 μs, whereas later times are defined as those that take up to 200 μs.

To provide a better insight into the submodel error behavior at the UFP, we first track the time evolution of each submodel for the particles initially located at the leftmost 0.5% of the particle curtain. Note that the order of the particles may change as the particle curtain moves and expands. Thus, the forces on the particle initially sitting on the UFP do not necessarily represent the forces on the particle located at the UFP over time. Figure 5 shows the time evolution of the force submodels (quasi-steady, pressure gradient, added-mass, and interparticle collisional forces) for the particle initially located at the leftmost 0.5% of the curtain during and after the shock interacts with the particle curtain at early times. The sudden change in the quasi-steady, pressure gradient, and added-mass force submodel during the first 2 μs is the result of crossing the shock over the particle. The interparticle collisional force submodel is small since the particle volume fraction (Fig. A1) stays small in the UFP region. The pressure gradient and added-mass force gradually diminish shortly after the shock leaves the UFP region.

Figure 6a shows the sensitivity indices of the UFP at early times, whereas Fig. 6b shows the same at later times. In the figure, four curves (quasi steady, pressure gradient, added mass, and the interparticle collisional) represent the first-order sensitivity indices, and the high-order terms' curve is the interaction effect between the model errors.

For the first 2 μs, when the shock just passed the UFP, the potential errors in the pressure gradient and added-mass forces dominate the variation in UFP. Shortly after that, however, the UFP variation is mostly affected by the potential error in the quasi-steady force. The initial magnitude of the pressure gradient and added-mass forces at the UFP during the first 10 μs is not negligible. However, the variation of the UFP is a cumulative effect of the errors over time. The combined effect of the pressure gradient and added-mass forces is negligible compared to the quasi-steady force because the values of the forces by themselves alter from positive to negative (Fig. 5) during the period. The effect of potential error in the interparticle collisional force on the variation of the UFP remains negligible for the entire simulation because the local particle volume fraction is generally small at the UFP. The initial distribution of the particle volume fraction follows a

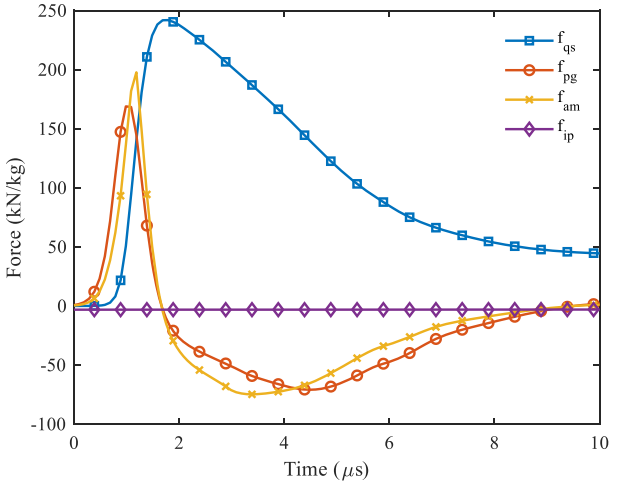

Fig. 5 Time evolution of the force submodels for the particle that is initially located at the UFP.

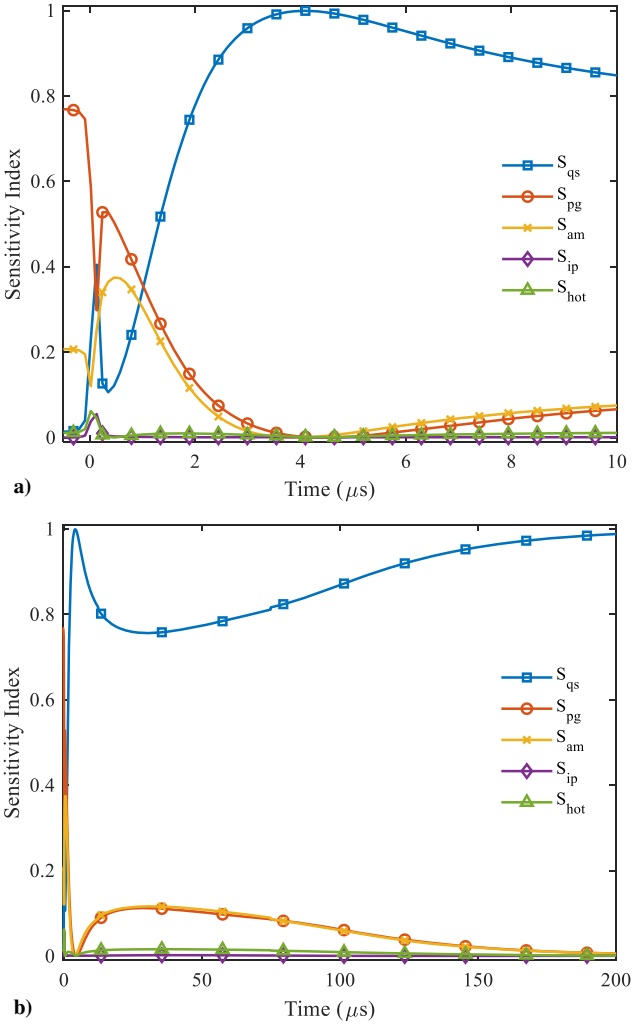

Fig. 6 Force submodel sensitivity indices for UFP a) at early times, and b) at later times.

Gaussian-shaped curve. Hence, a small local particle volume fraction corresponds to a negligible interparticle collisional force. The particle curtain expands over time, especially in the UFP region. The effects of pressure gradient and added-mass forces are gradually diminished after 150 μs, and the only error contribution that affects the UFP is the error in the quasi-steady force submodel.

Similar to the UFP, to provide a better insight into the submodel error behavior at the DFP, we track the time evolution of each submodel at the particles initially located at the rightmost 0.5% of the particle curtain. Figure 7 shows the time evolution of the force submodels for the particle initially located at the rightmost 0.5% of the curtain during and after the shock interacts with the particle curtain at early times. The sudden change in the quasi-steady, pressure gradient, and added-mass force submodels during the first few microseconds is the result of crossing the shock over the particle. Unlike the UPF, the interparticle collisional force is not negligible. A sudden fluctuation of the interparticle collisional force indicates a relatively large volume fraction due to the accumulation of the particles at the DFP (Fig. A1).

Figure 8 shows the sensitivity indices of the DFP in early times. The added-mass force sensitivity index suddenly spikes right after the shock crosses over the DFP because of the relatively large acceleration of the flow compared with the adjacent particles at the DFP. However, the initial rise in the pressure gradient force sensitivity index is small compared with that of the added-mass force because of the effect of two-way coupling when the particles try to push back the flow. Hence, the pressure drops at the DFP. As soon as the shock passes the DFP, the added-mass force drops, and its potential error contribution to the DFP variation becomes small. After the shock passes the DFP, the contribution of the potential error in the quasi-steady force submodel

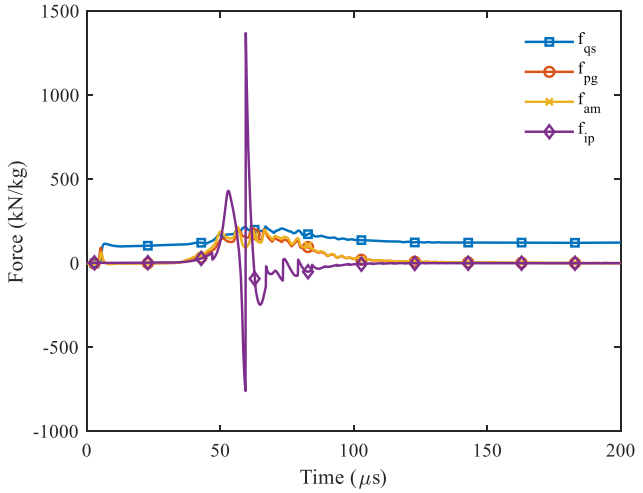

Fig. 7 Time evolution of the force submodels for the particle that initially is located at the DFP.

dominates the variation in the DFP. The contribution of the error in the quasi-steady force remains dominant until around $t = 55$ μs, where two interesting and related effects influence the particle forces and their sensitivity:

1) As can be seen in the particle volume fraction plots shown in Fig. A1, the particle volume fraction rapidly increases at the DFP. This increase in volume fraction is associated with an increase in pressure at the DFP and contributes to a substantial increase in the pressure gradient and the added-mass forces (Fig. 7).

2) As a result of the increased volume fraction, the interparticle collisional force starts rising rapidly as well (Fig. 7). The local particle volume fraction increases at the DFP because of instability driven by the volume fraction dependence of the force model in Eq. (2), which has been well established in the fluidized bed literature [54]. As the local particle volume fraction starts increasing, the effect of error in interparticle collisional force on the DFP variation slightly rises for a short time. Note that the rise of the interparticle collisional submodel sensitivity index is due to the cumulative effect of its variation on DFP. Thus, a slight sudden increase in the interparticle collisional submodel is a consequence of a relatively large fluctuation of the submodel (Fig. 7). Since the interparticle collisional force submodel in Eq. (5) heavily depends on the particle volume fraction, the increase in particle volume fraction at $t = 55$ μs leads to a drastic change in the interparticle collisional force. The force becomes weaker because the particle volume fraction decreases as the curtain expands, and the particle volume fraction becomes smaller. Simultaneously, the error contribution of the added-mass force and pressure gradient increases. The flow accelerates because of the increase in local particle volume fraction at the DFP. As a result, this increases the relative acceleration of the flow compared with the particles at the DFP, as well as the pressure gradient. Unlike the UPF, this effect of error in the pressure gradient and added-mass force does not disappear in a short time. As the particle curtain expands and the particles decelerate, the pressure gradient and added-mass force become smaller. Despite a very small pressure gradient and added-mass force magnitude after $t = 150$ μs, their effect remains nonzero for a much longer duration because the cumulative effect of the force submodels dictates the behavior of the sensitivity indices.

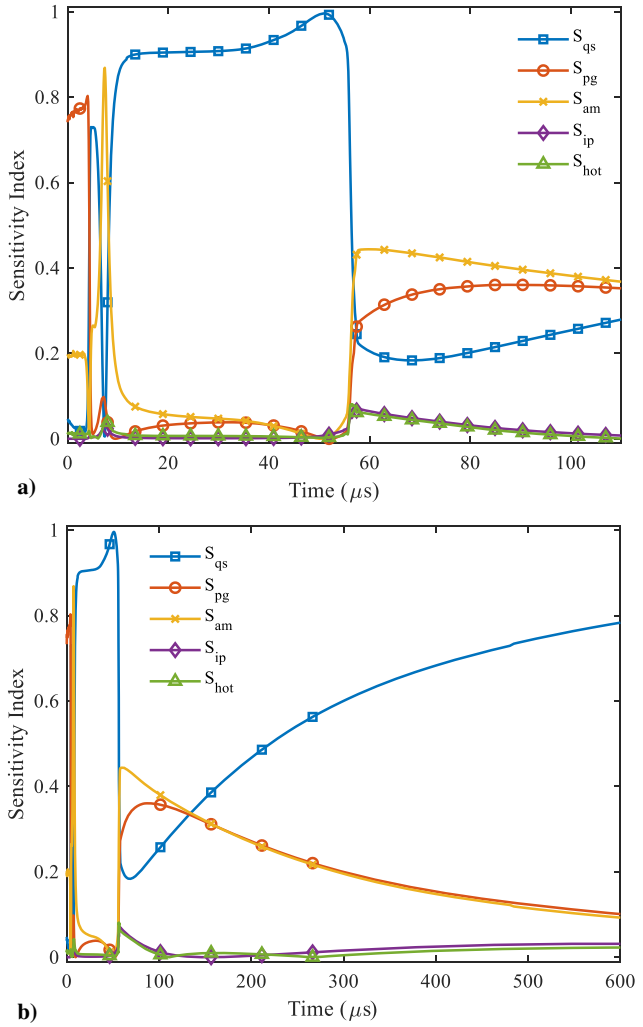

Fig. 8 Force submodels sensitivity indices for DFP a) at early times, and b) at later times.

The potential error in the quasi-steady force is identified as the main contributor to the variation of the UFP. The UFP is not sensitive to the potential error in the pressure gradient and added-mass force. The variation in the early motion of the DFP is mainly dictated by the potential error in the pressure gradient and added-mass force, whereas the long-time variation in the DFP depends on the potential error in the quasi-steady, pressure gradient, and added-mass forces. Figures 9a and 9b illustrate a hypothetical scenario where the quasi-steady, pressure gradient, and added-mass force submodels are modified as −10, 50, and 50%, leading to compensation for the potential errors in the original model.

The solid and the dashed–dotted lines in Figs. 9a and 9b represent the average values for the experimental measurement and the simulation prediction, respectively, which have already been shown in Fig. 3. The dashed line is the predicted UFP and DFP when the possible submodel errors are corrected. It is noted that the numerical simulation is more agreeable with the experimental measurement after the correction. Note also that this correction simply gives us a clue in identifying the most important error contributors. The preceding illustration does not mean that the force submodels necessarily have these precise error bounds. Simply, the GSA results in rank and isolates the contribution of error in each submodel to the error in the model prediction.

VII. Conclusions

This paper studied the potential epistemic drag force model error in the context of one-dimensional numerical simulation of compressible multiphase dispersed flow. The drag force model is composed of several submodels (quasi-steady, pressure gradient, added-mass, and interparticle collisional forces), where each submodel processes a potential epistemic error. The model output error comes from the combined effect of the possible error on each submodel. Since the submodel errors can add up or compensate for one another over time, it is difficult to identify the major source of errors. The contribution of this paper is to quantify the contribution of each submodel error to the model output error. For this purpose, a constant error bound was assumed for each submodel and global sensitivity analysis was used as a tool to prioritize the importance of the potential error on each submode.

It was found that if looking forward to reducing the uncertainty of the UFP, investment in the improvement of the quasi-steady force

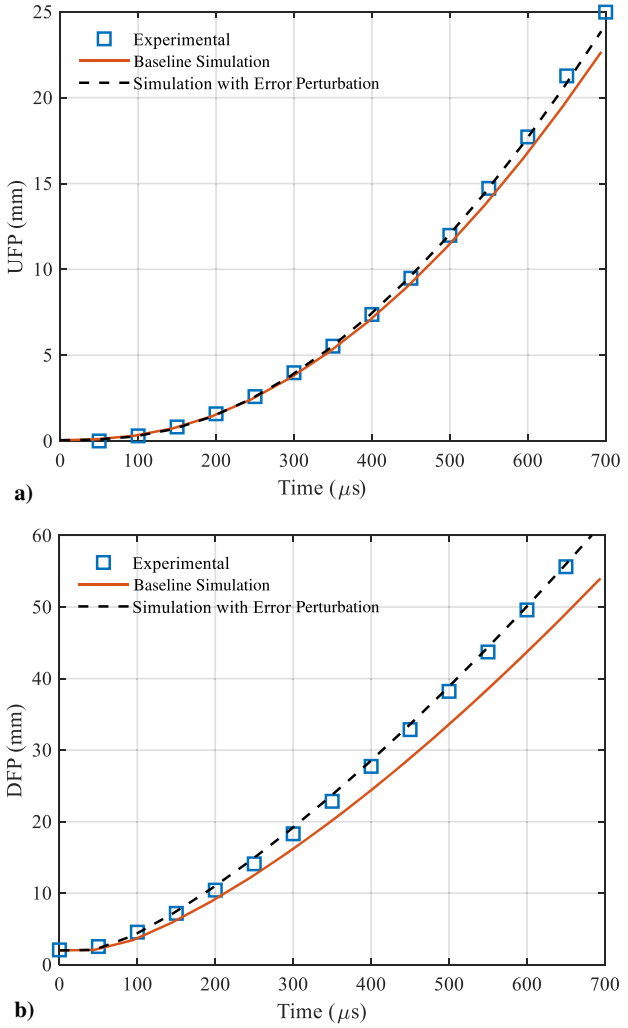

Fig. 9 Change in the front particle motion after error perturbation vs the experimental measurement: a) UFP, and b) DFP.

submodel must be made. If interested in improving the accuracy of the DFP prediction for a very short time, again, the improvement on the quasi-steady model is essential. For a long-term prediction of the DFP, the improvement of quasi-steady, pressure gradient, and added-mass forces is needed. The effect of the error in the interparticle collisional force model cannot be neglected because this force mainly dictates the particle clustering effect, and it plays a vital role on the long-term effect of the pressure gradient and added-mass force. Otherwise, unrealistic results for the long-term effect of the pressure gradient and added-mass force on the DFP variation might occur due to the poor interparticle collisional force model. Nili et al. [28] performed a preliminary version of this study with a top-hat initial particle volume fraction profile. The different values of the initial particle volume fraction resulted in a different trend for the potential influence of the interparticle collisional force submodel on the particle front variation. Consequently, they changed the possible long-term effect of error in the other force submodels.

Appendix: Distribution of Particle Volume Fraction

The initial particle volume fraction that we use for the simulation follows a Gaussian distribution. We constructed the input particle volume fraction profile based on a linear regression model with correlated noise using a Gaussian process, which developed by Park et al. [55]. The model is inspired by the experimental x-ray measurement conducted by Wagner et al. [22]. Figure 8 shows the time evolution of particle volume fraction in different timeframes after the shock hits the particle curtain. The solid line represents the initial particle volume fraction, whose maximum value is 21%. The particle

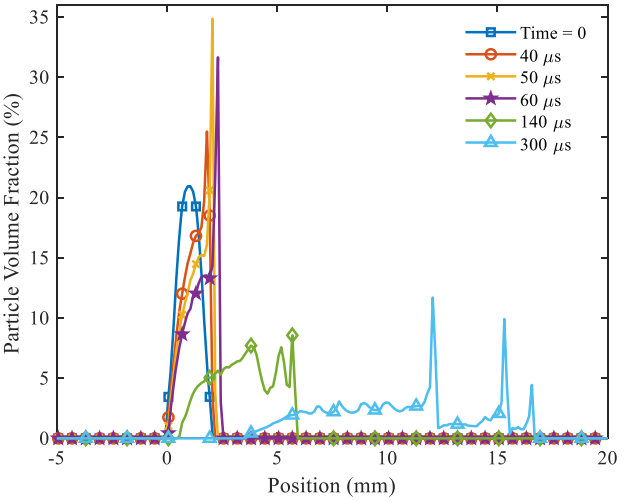

Fig. A1 Time evolution of particle volume fraction.

curtain moves and expands because of aerodynamic and interparticle collisional forces. Shortly after the shock passes over the curtain, the particles start to form a cluster at the DFP. Each spike on the particle volume fraction profile represents a particle cluster. For example, the line marked with a square symbol in Fig. A1 shows a spike (cluster) that already formed at the DFP about 40 μs after the shock passed over the UFP. At the downstream particle front, the cluster is formed in the following manner: The local particle volume fraction increases at the DFP due to an instability driven by the volume fraction dependence of the force model in Eq. (2). Consider a narrow layer of higher volume fraction within the curtain sandwiched between regions of the lower volume fraction. The particles within this region of higher volume fraction experience a higher drag and move faster. As they run over the slower-moving particles, a region of yet higher volume fraction results. This leads to a further increase in velocity and further absorption of particles from upstream. The number of the clusters increases as the particle curtain expands and moves, and it propagates upstream into the main body of the particle curtain. Further details about this behavior are available in the work of Nili [23].

Acknowledgments

This work supported by the U.S. Department of Energy, NNSA, Advanced Simulation and Computing Program as a cooperative agreement under the Predictive Science Academic Alliance Program (PSAAP II), contract no. DE-NA0002378.

References

[1] Wagner, J. L., Beresh, S. J., Kearney, S. P., Pruett, B. O., and Wright, E. K., "Shock Tube Investigation of Quasi-Steady Drag in Shock–Particle Interactions," *Physics of Fluids*, Vol. 24, No. 12, 2012, Paper 123301. https://doi.org/10.1063/1.4768816

[2] Wagner, J. L., Beresh, S. J., Kearney, S. P., Trott, W. M., Castaneda, J. N., Pruett, B. O., and Baer, M. R., "A Multiphase Shock Tube for Shock Wave Interactions with Dense Particle Fields," *Experiments in Fluids*, Vol. 52, No. 6, 2012, pp. 1507–1517. https://doi.org/10.1007/s00348-012-1272-x

[3] Saltelli, A., Tarantola, S., Campolongo, F., and Ratto, M., *Sensitivity Analysis in Practice: A Guide to Assessing Scientific Models*, Wiley, New York, 2004. https://doi.org/10.1002/0470870958

[4] Saltelli, A., "Sensitivity Analysis: Could Better Methods Be Used?" *Journal of Geophysical Research: Atmospheres*, Vol. 104, No. D3, 1999, pp. 3789–3793. https://doi.org/10.1029/1998JD100042

[5] McKay, M. D., Beckman, R. J., and Conover, W. J., "Comparison of Three Methods for Selecting Values of Input Variables in the Analysis of Output from a Computer Code," *Technometrics*, Vol. 21, No. 2, 1979, pp. 239–245. https://doi.org/10.2307/1268522

[6] Cukier, R., Levine, H., and Shuler, K., "Nonlinear Sensitivity Analysis of Multiparameter Model Systems," *Journal of Computational Physics*, Vol. 26, No. 1, 1978, pp. 1–42. https://doi.org/10.2307/1268522

[7] Saltelli, A., Tarantola, S., and Chan, K.-S., "A Quantitative Model-Independent Method for Global Sensitivity Analysis of Model Output," *Technometrics*, Vol. 41, No. 1, 1999, pp. 39–56. https://doi.org/10.1080/00401706.1999.10485594

[8] Saltelli, A., and Sobol, I. M., "About the Use of Rank Transformation in Sensitivity Analysis of Model Output," *Reliability Engineering and System Safety*, Vol. 50, No. 3, 1995, pp. 225–239. https://doi.org/10.1016/0951-8320(95)00099-2

[9] Archer, G., Saltelli, A., and Sobol, I., "Sensitivity Measures, ANOVA-Like Techniques and the Use of Bootstrap," *Journal of Statistical Computation and Simulation*, Vol. 58, No. 2, 1997, pp. 99–120. https://doi.org/10.1080/00949659708811825

[10] Sobol, I. M., "Sensitivity Estimates for Nonlinear Mathematical Models," *Mathematical Modelling and Computational Experiments*, Vol. 1, No. 4, 1993, pp. 407–414.

[11] Matsumura, T., Haftka, R. T., and Sankar, B. V., "Reliability Estimation Including Redesign Following Future Test for an Integrated Thermal Protection System," *Proceedings of 9th World Congress on Structural and Multidisciplinary Optimization*, International Soc. of Structural and Multidisciplinary Optimization, Shizuoka, Japan, June 2011, pp. 14–17

[12] Matsumura, T., and Haftka, R. T., "Reliability Based Design Optimization Modeling Future Redesign with Different Epistemic Uncertainty Treatments," *Journal of Mechanical Design*, Vol. 135, No. 9, 2013, Paper 091006. https://doi.org/10.1115/1.4024726

[13] Zhang, R., and Mahadevan, S., "Model Uncertainty and Bayesian Updating in Reliability-Based Inspection," *Structural Safety*, Vol. 22, No. 2, 2000, pp. 145–160. https://doi.org/10.1016/S0167-4730(00)00005-9

[14] Sankararaman, S., Ling, Y., and Mahadevan, S., "Uncertainty Quantification and Model Validation of Fatigue Crack Growth Prediction," *Engineering Fracture Mechanics*, Vol. 78, No. 7, 2011, pp. 1487–1504. https://doi.org/10.1016/j.engfracmech.2011.02.017

[15] Burt, J. M., and Josyula, E., "Global Sensitivity Analysis and Uncertainty Quantification for a Hypersonic Shock Interaction Flow," *Journal of Thermophysics and Heat Transfer*, Vol. 29, No. 3, 2015, pp. 439–449. https://doi.org/10.2514/1.T4368

[16] Youn, B. D., Jung, B. C., Xi, Z., Kim, S. B., and Lee, W., "A Hierarchical Framework for Statistical Model Calibration in Engineering Product Development," *Computer Methods in Applied Mechanics and Engineering*, Vol. 200, Nos. 13–16, 2011, pp. 1421–1431. https://doi.org/10.1016/j.cma.2010.12.012

[17] Jung, B. C., Yoon, H., Oh, H., Lee, G., Yoo, M., Youn, B. D., and Huh, Y. C., "Hierarchical Model Calibration for Designing Piezoelectric Energy Harvester in the Presence of Variability in Material Properties and Geometry," *Structural and Multidisciplinary Optimization*, Vol. 53, No. 1, 2016, pp. 161–173. https://doi.org/10.1007/s00158-015-1310-4

[18] Sankararaman, S., McLemore, K., Mahadevan, S., Bradford, S. C., and Peterson, L. D., "Test Resource Allocation in Hierarchical Systems Using Bayesian Networks," *AIAA Journal*, Vol. 51, No. 3, 2013, pp. 537–550. https://doi.org/10.2514/1.J051542

[19] Sridharan, P., Jackson, T. L., Zhang, J., and Balachandar, S., "Shock Interaction with One-Dimensional Array of Particles in Air," *Journal of Applied Physics*, Vol. 117, No. 7, 2015, Paper 075902. https://doi.org/10.1063/1.4913217

[20] Mehta, Y., Jackson, T., Zhang, J., and Balachandar, S., "Numerical Investigation of Shock Interaction with One-Dimensional Transverse Array of Particles in Air," *Journal of Applied Physics*, Vol. 119, No. 10, 2016, Paper 104901. https://doi.org/10.1063/1.4943616

[21] Mehta, Y., Neal, C., Jackson, T., Balachandar, S., and Thakur, S., "Shock Interaction with Three-Dimensional Face Centered Cubic Array of Particles," *Physical Review Fluids*, Vol. 1, No. 5, 2016, Paper 054202. https://doi.org/10.1103/PhysRevFluids.1.054202

[22] Wagner, J. L., Kearney, S. P., Beresh, S. J., DeMauro, E. P., and Pruett, B. O., "Flash X-Ray Measurements on the Shock-Induced Dispersal of a Dense Particle Curtain," *Experiments in Fluids*, Vol. 56, No. 12, 2015, p. 213. https://doi.org/10.1007/s00348-015-2087-3

[23] Nili, S., "Error Analysis of Particle Force Model of an Euler–Lagrange Multiphase Dispersed Flow," Ph.D. Dissertation, Univ. of Florida, Belle Glade, FL, 2019, https://ufdc.ufl.edu/UFE0055661/00001 [retrieved 27 Feb. 2021].

[24] Center for Simulation ofAdvanced Rockets (CSAR), Univ. of Illinois Urbana-Champaign, Urbana, IL, 2002, http://charm.cs.uiuc.edu/kale/csarOct02/0_SOWAllText.pdf [retrieved 27 Feb. 2021].

[25] Ling, Y., Wagner, J., Beresh, S., Kearney, S., and Balachandar, S., "Interaction of a Planar Shock Wave with a Dense Particle Curtain: Modeling and Experiments," *Physics of Fluids*, Vol. 24, No. 11, 2012, Paper 113301. https://doi.org/10.1063/1.4768815

[26] Park, C., Nili, S., Mathew, J. T., Kim, N. H., and Haftka, R. T., "Uncertainty Investigation for Shock Tube Simulation Error Quantification," *2018 AIAA Non-Deterministic Approaches Conference*, AIAA Paper 2018-1662, 2018. https://doi.org/10.2514/6.2018-1662

[27] Park, C., Nili, S., Matthew, J., Kim, N. H., and Haftka, R. T., "Uncertainty Reduction for Model Error Detection in Multiphase Shock Tube Simulation," *Journal of Verification, Validation and Uncertainty Quantification* (in press).

[28] Nili, S., Park, C., Haftka, R. T., Balachandar, S., and Kim, N. H., "Sensitivity Analysis of Force Models for a Four-Way Coupled Eulerian–Lagrangian Dispersed Multiphase Flow," *23rd AIAA Computational Fluid Dynamics Conference*, AIAA Paper 2017-3800, 2017. https://doi.org/10.2514/6.2017-3800

[29] Maxey, M. R., and Riley, J. J., "Equation of Motion for a Small Rigid Sphere in a Nonuniform Flow," *Physics of Fluids*, Vol. 26, No. 4, 1983, pp. 883–889. https://doi.org/10.1063/1.864230

[30] Parmar, M., Haselbacher, A., and Balachandar, S., "Generalized Basset-Boussinesq-Oseen Equation for Unsteady Forces on a Sphere in a Compressible Flow," *Physical Review Letters*, Vol. 106, No. 8, 2011, Paper 084501. https://doi.org/10.1103/PhysRevLett.106.084501

[31] Parmar, M., Haselbacher, A., and Balachandar, S., "Equation of Motion for a Sphere in Non-Uniform Compressible Flows," *Journal of Fluid Mechanics*, Vol. 699, May 2012, pp. 352–375. https://doi.org/10.1017/jfm.2012.109

[32] Annamalai, S., and Balachandar, S., "Faxén Form of Time-Domain Force on a Sphere in Unsteady Spatially Varying Viscous Compressible Flows," *Journal of Fluid Mechanics*, Vol. 816, April 2017, pp. 381–411. https://doi.org/10.1017/jfm.2017.77

[33] Houim, R. W., and Oran, E. S., "A Multiphase Model for Compressible Granular–Gaseous Flows: Formulation and Initial Tests," *Journal of Fluid Mechanics*, Vol. 789, Feb. 2016, pp. 166–220. https://doi.org/10.1017/jfm.2015.728

[34] Liu, H., Guo, Y., and Lin, W., "Simulation of Shock-Powder Interaction Using Kinetic Theory of Granular Flow," *Powder Technology*, Vol. 273, March 2015, pp. 133–144. https://doi.org/10.1016/j.powtec.2014.12.031

[35] Ling, Y., Haselbacher, A., and Balachandar, S., "Importance of Unsteady Contributions to Force and Heating for Particles in Compressible Flows. Part 2: Application to Particle Dispersal by Blast Waves," *International Journal of Multiphase Flow*, Vol. 37, No. 9, 2011, pp. 1013–1025. https://doi.org/10.1016/j.ijmultiphaseflow.2011.07.002

[36] Ling, Y., Haselbacher, A., and Balachandar, S., "Importance of Unsteady Contributions to Force and Heating for Particles in Compressible Flows: Part 1: Modeling and Analysis for Shock–Particle Interaction," *International Journal of Multiphase Flow*, Vol. 37, No. 9, 2011, pp. 1026–1044. https://doi.org/10.1016/j.ijmultiphaseflow.2011.07.001

[37] Parmar, M., Haselbacher, A., and Balachandar, S., "Modeling of the Unsteady Force for Shock–Particle Interaction," *Shock Waves*, Vol. 19, No. 4, 2009, pp. 317–329. https://doi.org/10.1007/s00193-009-0206-x

[38] Magnaudet, J., and Eames, I., "The Motion of High-Reynolds-Number Bubbles in Inhomogeneous Flows," *Annual Review of Fluid Mechanics*, Vol. 32, No. 1, 2000, pp. 659–708. https://doi.org/10.1146/annurev.fluid.32.1.659

[39] Balachandar, S., and Eaton, J. K., "Turbulent Dispersed Multiphase Flow," *Annual Review of Fluid Mechanics*, Vol. 42, Jan. 2010, pp. 111–133. https://doi.org/10.1146/annurev.fluid.010908.165243

[40] Harris, S., and Crighton, D., "Solitons, Solitary Waves, and Voidage Disturbances in Gas-Fluidized Beds," *Journal of Fluid Mechanics*, Vol. 266, May 1994, pp. 243–276. https://doi.org/10.1017/S0022112094000996

[41] Enwald, H., Peirano, E., and Almstedt, A.-E., "Eulerian Two-Phase Flow Theory Applied to Fluidization," *International Journal of Multiphase Flow*, Vol. 22, Dec. 1996, pp. 21–66. https://doi.org/10.1016/S0301-9322(96)90004-X

[42] Choi, K. K., and Kim, N.-H., *Structural Sensitivity Analysis and Optimization 1: Linear Systems*, Springer Science and Business Media, New York, 2006. https://doi.org/10.1007/b138709

[43] Skene, C. S., and Schmid, P. J., "Adjoint-Based Parametric Sensitivity Analysis for Swirling M-Flames," *Journal of Fluid Mechanics*, Vol. 859, Jan. 2019, pp. 516–542.
https://doi.org/10.1017/jfm.2018.793

[44] Giannetti, F., Camarri, S., and Citro, V., "Sensitivity Analysis and Passive Control of the Secondary Instability in the Wake of a Cylinder," *Journal of Fluid Mechanics*, Vol. 864, April 2019, pp. 45–72.
https://doi.org/10.1017/jfm.2019.17

[45] Ganguly, V., Kim, N. H., Kim, H. S., and Schmitz, T., "Sensitivity Analysis of Periodic Errors in Heterodyne Interferometry," *Measurement Science and Technology*, Vol. 22, No. 3, 2011, Paper 035305.
https://doi.org/10.1088/0957-0233/22/3/035305

[46] Hosder, S., and Bettis, B., "Uncertainty and Sensitivity Analysis for Reentry Flows with Inherent and Model-Form Uncertainties," *Journal of Spacecraft and Rockets*, Vol. 49, No. 2, 2012, pp. 193–206.
https://doi.org/10.2514/1.A32102

[47] Pei, Y., Davis, M. J., Pickett, L. M., and Som, S., "Engine Combustion Network (ECN): Global Sensitivity Analysis of Spray A for Different Combustion Vessels," *Combustion and Flame*, Vol. 162, No. 6, 2015, pp. 2337–2347.
https://doi.org/10.1016/j.combustflame.2015.01.024

[48] Liang, B., and Mahadevan, S., "Error and Uncertainty Quantification and Sensitivity Analysis in Mechanics Computational Models," *International Journal for Uncertainty Quantification*, Vol. 1, No. 2, 2011, pp. 147–161.
https://doi.org/10.1615/Int.J.UncertaintyQuantification.v1.i2.30

[49] Higdon, K. J., Goldstein, D. B., and Varghese, P. L., "Sensitivity Analysis of Direct Simulation Monte Carlo Parameters for Ionizing Hypersonic Flows," *Journal of Thermophysics and Heat Transfer*, Vol. 32, No. 1, 2017, pp. 90–102.
https://doi.org/10.2514/1.T5094

[50] Jiang, Z., Chen, W., and German, B. J., "Multidisciplinary Statistical Sensitivity Analysis Considering Both Aleatory and Epistemic Uncertainties," *AIAA Journal*, Vol. 54, No. 4, 2016, pp. 1326–1338.
https://doi.org/10.2514/1.J054464

[51] Huan, X., Safta, C., Sargsyan, K., Geraci, G., Eldred, M. S., Vane, Z. P., Lacaze, G., Oefelein, J. C., and Najm, H. N., "Global Sensitivity Analysis and Estimation of Model Error, Toward Uncertainty Quantification in Scramjet Computations," *AIAA Journal*, Vol. 56, No. 3, 2018, pp. 1170–1184.
https://doi.org/10.2514/1.J056278

[52] Xiong, Y., Chen, W., Apley, D., and Ding, X., "A Non-Stationary Covariance–Based Kriging Method for Metamodelling in Engineering Design," *International Journal for Numerical Methods in Engineering*, Vol. 71, No. 6, 2007, pp. 733–756.
https://doi.org/10.1002/nme.1969

[53] Kleijnen, J. P., "Regression and Kriging Metamodels with Their Experimental Designs in Simulation: A Review," *European Journal of Operational Research*, Vol. 256, No. 1, 2017, pp. 1–16.
https://doi.org/10.1016/j.ejor.2016.06.041

[54] Sundaresan, S., "Instabilities in Fluidized Beds," *Annual Review of Fluid Mechanics*, Vol. 35, No. 1, 2003, pp. 63–88.
https://doi.org/10.1146/annurev.fluid.35.101101.161151

[55] Park, C., Matthew, J., Kim, N. H., and Haftka, R. T., "Epistemic Uncertainty Stemming From Measurement Processing—A Case Study of Multiphase Shock Tube Experiments," *Journal of Verification, Validation and Uncertainty Quantification*, Vol. 3, No. 4, 2018, Paper 041001.
https://doi.org/10.1115/1.4042814

R. Ghanem
Associate Editor